INTERNATIONAL JOURNAL FOR NUMERICAL METHODS IN FLUIDS
Int. J. Numer. Meth. Fluids 2004; **45**:1161–1186 (DOI: 10.1002/fld.632)

Efficient and accurate time adaptive multigrid simulations of droplet spreading

P. H. Gaskell[1,*,†], P. K. Jimack[2], M. Sellier[1] and H. M. Thompson[1]

[1]*Engineering Fluid Mechanics Research Group, School of Mechanical Engineering, The University of Leeds, Leeds LS2 9JT, U.K.*
[2]*School of Computing, The University of Leeds, Leeds LS2 9JT, U.K.*

SUMMARY

An efficient full approximation storage (FAS) Multigrid algorithm is used to solve a range of droplet spreading flows modelled as a coupled set of non-linear lubrication equations. The algorithm is fully implicit and has embedded within it an adaptive time-stepping scheme that enables the same to be optimized in a controlled manner subject to a specific error tolerance. The method is first validated against a range of analytical and existing numerical predictions commensurate with droplet spreading and then used to simulate a series of new, three-dimensional flows consisting of droplet motion on substrates containing topographic and wetting heterogeneities. The latter are of particular interest and reveal how droplets can be made to spread preferentially on substrates owing to an interplay between different topographic and surface wetting characteristics. Copyright © 2004 John Wiley & Sons, Ltd.

KEY WORDS: droplets; spreading; multigrid; adaptive time-stepping; lubrication approximation; fully implicit

1. INTRODUCTION

The focus of this paper is the efficient numerical solution of flows involving droplet spreading through the use of a fully implicit, time-adaptive Multigrid algorithm. Such flows are of enormous significance in many branches of science and commerce, industrial applications including, for example, the deposition of coatings and inks, direct patterning of functional layers during microship production, spreading of pesticides and the flow of oil in heat exchangers [1, 2]. The same also arise in other diverse areas of science ranging from biology, where they form membranes on mammalian lungs and tear films in the eye, to geology where they feature in lava flows [3].

Problems are modelled using a long wave, or *lubrication*, approximation with the advantage that proceeding in this way reduces the dimensionality by one and yields more tractable

*Correspondence to: P. H. Gaskell, Engineering Fluid Mechanics Research Group, School of Mechanical Engineering, University of Leeds, Leeds LS2 9JT, U.K.
† E-mail: p.h.gaskell@efm.leeds.ac.uk

Published online 25 May 2004

Received 9 November 2002
Revised 30 June 2003

fourth-order partial differential equations (p.d.e.s) than encountered in a full Navier–Stokes formulation. Despite this simplification, significant obstacles remain to be overcome, principally due to the stiffness introduced by surface tension and the need to resolve short length scales close to wetting lines. Similarly, explicit time stepping numerical schemes are of limited value since they suffer an impractical restriction apropos the time step, Δt, which must be at most $O(\Delta^4)$, where Δ is the spatial resolution, to avoid numerical instability [4].

Several authors have solved the time-dependent lubrication equations successfully in a wide variety of physical contexts. Prominent among these have been the studies of Schwartz and co-workers who have eased the severe restriction on time step noted above by employing alternating-direction implicit (ADI) algorithms which, for three-dimensional flows, use alternating sweeps in each direction so that only a banded system of equations need be solved at each time step [5]. These schemes, often referred to as *time-splitting* [6], have been used to analyse a range of problems including, for example, those due to the effects of substrate curvature and surface tension gradients on the thinning of coatings [7], droplet motions on heterogeneous substrates with materials having widely different equilibrium contact angles [8, 9] and gravity- and surface shear stress-driven thin coating flows [10]. In all of these studies, spreading motion is facilitated by specifying a thin energetically stable wetting layer, or *precursor film*, of thickness h^* over the surface of the substrate, an approach that has significant computational advantages over alternative, slip models [11, 12].

In contrast to time-splitting, Multigrid methods are fast solvers, originally developed for the solution of elliptic p.d.e.s. Their essence is to use a simple iterative technique as a smoother, not as a solver, on a sequence of computational grids to reduce high frequency error components on a particular grid [13]. They have been applied to increasingly difficult systems of p.d.e.s and are now commonly used to solve the discrete analogues arising from a wide variety of flow problems for which major improvements in efficiency and robustness are being achieved [14–17]. The full approximation storage (FAS) variant of the Multigrid method for non-linear equations [18] is implemented to solve a suitable finite difference approximation to the time-dependent lubrication equations for the flow of droplets over substrates either with or without wetting and/or the presence of topographic heterogeneities. Embedded within the algorithm is an efficient, adaptive time-stepping scheme, based on Heun's second-order predictor–corrector method [19], which automatically adjusts the time step subject to a specified error tolerance enabling Δt to be optimized in a controlled manner.

A compact derivation of the governing equations to be solved is presented for completeness, followed by details of the underpinning numerical method(s) adopted for their solution. The Multigrid solver is first validated against a range of analytical and previously published numerical predictions for droplet spreading phenomena and then extended to simulate a variety of spreading flows on substrate with different wettability characteristics and containing topographic features.

2. MATHEMATICAL MODEL

Figure 1 is a schematic snap-shot of the flow of a droplet, $H(X, Y, T)$, over a topographic feature, $S(X, Y)$, of amplitude S_0 and lengths L_T and W_T with respect to the reference co-ordinate (X, Y) on a substrate inclined at an angle α to the horizontal. Its aspect ratio $A = W_T/L_T$. The fluid is Newtonian and incompressible, of density ρ and viscosity μ, and Marangoni effects are

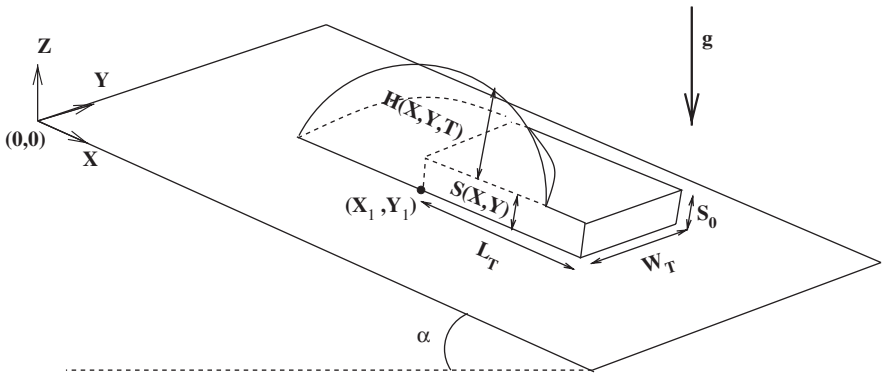

Figure 1. Schematic snap-shot of the flow of a droplet, $H(X, Y, T)$, over a topography, $S(X, Y)$, on a substrate inclined at an angle α to the horizontal, showing a section through the droplet for the sake of clarity, in the X–Z plane and the parameters defining the topography.

ignored so that the surface tension, σ, is also constant. The motion of the droplet is governed by the time-dependent Navier–Stokes equations, viz

$$\rho\left(\frac{\partial \underline{U}}{\partial t} + \underline{U}.\nabla\underline{U}\right) = -\nabla P + \mu\nabla^2\underline{U} + \rho\underline{g} \tag{1}$$

$$\nabla.\underline{U} = 0 \tag{2}$$

where $\underline{U} = (U, V, W)$ and P are the fluid velocity and pressure, respectively, and $\underline{g} = g(\sin\alpha, 0, -\cos\alpha)$, where $g = 9.81\text{ms}^{-2}$ is the acceleration due to gravity. Taking H_0 as the characteristic droplet thickness and L_0 as the extent of the substrate, it is assumed that $\varepsilon = H_0/L_0$ is small so that the Navier–Stokes equations can be simplified using the long-wave, or *lubrication*, approximation. All analyses are performed and results presented in terms of corresponding non-dimensional (lower case) variables, the key ones being:

$$h(x, y, t) = \frac{H(X, Y, T)}{H_0}, \quad s(x, y) = \frac{S(X, Y)}{H_0}, \quad (x, y) = \frac{(X, Y)}{L_0}, \quad z = \frac{Z}{H_0}$$

$$p = \frac{L_0 P}{\sigma\varepsilon}, \quad \left(u, v, \frac{w}{\varepsilon}\right) = (U, V, W)\frac{T_0}{L_0}, \quad t = \frac{T}{T_0}, \quad T_0 = \frac{\mu L_0}{\sigma\varepsilon^3} \tag{3}$$

where the time scale T_0 is that derived by Orchard [20] for the levelling of surface disturbances. Note that since the substrate surface is given by the topography function $s(x, y)$ so that the droplet lies between $z = s$ and $h + s$. Under the above non-dimensionalization, neglecting terms of $O(\varepsilon^2)$ or higher, the Navier–Stokes equations reduce to

$$\frac{\partial^2 u}{\partial z^2} = \frac{\partial p}{\partial x} - \frac{B_o}{\varepsilon}\sin\alpha \tag{4}$$

$$\frac{\partial^2 v}{\partial z^2} = \frac{\partial p}{\partial y} \tag{5}$$

$$\frac{\partial p}{\partial z} = -B_o \cos\alpha \tag{6}$$

where $B_o = \rho g L_0^2/\sigma$ is the Bond number measuring the relative importance of gravitational to surface tension forces. These equations are solved subject to the condition of no-slip at the surface of the substrate and zero tangential stress at the free surface of the droplet, namely

$$(u, v) = (0, 0) \text{ at } z = s \quad \text{and} \quad \frac{\partial u}{\partial z} = \frac{\partial v}{\partial z} = 0 \text{ at } z = h + s \tag{7}$$

Equations (4) and (5) integrated twice with respect to z over the droplet thickness $z \in [s, h+s]$ and, subject to the above boundary conditions, yield

$$u = \left(\frac{\partial p}{\partial x} - \frac{B_o}{\varepsilon}\sin\alpha\right)(z-s)\left(\frac{1}{2}(z-s) - h\right) \tag{8}$$

$$v = \left(\frac{\partial p}{\partial y}\right)(z-s)\left(\frac{1}{2}(z-s) - h\right) \tag{9}$$

The time-dependent lubrication equation for the evolution of the droplet thickness is obtained by conserving mass throughout the flow, viz

$$\frac{\partial h}{\partial t} = -\nabla.\underline{\underline{Q}} \tag{10}$$

where $\underline{\underline{Q}} = \int_s^{h+s} (u, v)^{\mathrm{T}}\, \mathrm{d}z$. Integrating Equations (8) and (9) to form $\underline{\underline{Q}}$ and substituting into Equation (10) yields the following equation in terms of the pressure field p:

$$\frac{\partial h}{\partial t} = \frac{\partial}{\partial x}\left[\frac{h^3}{3}\left(\frac{\partial p}{\partial x} - \frac{B_o}{\varepsilon}\sin\alpha\right)\right] + \frac{\partial}{\partial y}\left[\frac{h^3}{3}\left(\frac{\partial p}{\partial y}\right)\right] \tag{11}$$

In common with the work of others [8, 9] a disjoining pressure term is employed to alleviate the singularity at wetting lines. This model assumes a thin precursor film of thickness h^* ahead of the same and relates the observed contact angle for partially wetting systems to intermolecular forces that become important for liquids of submicroscopic dimensions [9]. The disjoining pressure term, $\Pi(h)$, is given [21] by

$$\Pi(h) = \frac{(n-1)(m-1)(1-\cos\Theta_{\mathrm{e}})}{h^*(n-m)\varepsilon^2}\left[\left(\frac{h^*}{h}\right)^n - \left(\frac{h^*}{h}\right)^m\right] \tag{12}$$

where n and m are the exponents of the interaction potential and $\Theta_{\mathrm{e}}(x, y)$ is the equilibrium contact angle. Note that the disjoining pressure term is zero for a fully wetting system since $\Theta_{\mathrm{e}} = 0$.

Experimental evidence suggests that, in practice, h^* lies in the range 1–100 nm [22] so that currently it is not feasible to use realistic h^* values in computations. This restriction has two ramifications. The first and most important is due to the fact that accurate representation

of a wetting line and, in particular, avoidance of negative film thicknesses in their vicinity requires that the spatial resolution should be of the same order of magnitude as h^*. This and related issues are discussed in detail by Bertozzi [4] and have led to the development of new numerical schemes which ensure that the film thickness remains positive without requiring excessive mesh refinement near wetting lines [23]. The second problem relates to the fact that h^* is the principal determinant of spreading rate [9]. However, although inability to use a sufficiently small h^* in computations leads to a systematic over-prediction of spreading rate, this difficulty can normally be compensated for by using an analytic correction [8].

The pressure field throughout the droplet is obtained by integrating Equation (6) with respect to z where the constant of integration (setting the pressure datum to atmospheric) is given by

$$p = -\nabla^2(h+s) - \Pi(h) \quad \text{on } z = h+s \tag{13}$$

where the $\nabla^2(h+s)$ term is the small slope approximation to the surface curvature of the thin film, leading to

$$p = -\nabla^2(h+s) - \Pi(h) + B_o \cos\alpha(h+s-z) \tag{14}$$

It is important to note that since the lubrication approximation is formally valid only for flows for which the free surface slope is small, its accuracy could be affected by the steep slopes of the topographies considered here. However, recent studies [24, 25] and comparison with experiment [2, 34] show lubrication theory to be remarkably robust in such circumstances providing the associated Reynolds and Capillary numbers are not too large. Note also that the form of Equation (11) ensures that the z dependence in Equation (14) has no influence on the evolution of the film thickness and it is therefore omitted from subsequent analysis.

Previous workers have simply substituted Equation (14) into Equation (11) to yield fourth-order time-dependent lubrication equations purely in terms of the film thickness, h. However in the present study it is found advantageous to solve the coupled non-linear equation set for h and p, Equations (11) and (14), respectively, since the second-order differential operators are simpler to discretize and a substrate wettability function $\Theta_e(x, y)$, for variably wettable substrates, can be imposed without imposing constraints on its differentiability [8].

Equations (11) and (14) are solved subject to symmetry boundary conditions at the edges of the computational domain, namely

$$\frac{\partial p}{\partial n} = \frac{\partial h}{\partial n} = 0 \tag{15}$$

where n is the normal to the substrate boundary.

3. NUMERICAL METHOD

3.1. Spatial discretization

All problems are solved on a square computational domain with $(x, y) \in \Omega = (0,1) \times (0,1)$ using a Multigrid approach. The finest grid level (i.e. the actual grid on which the solution is desired) has $(2^{k_f}+1)$ nodes in each direction so that the spatial co-ordinates of its grid points are given by $x_i = (i-1)/2^{k_f}$ and $y_j = (j-1)/2^{k_f}$ in terms of the fine grid density parameter

k_f. In the present study $k_f \in [6, 10]$ corresponding to grids at the finest level with between 65 and 1025 nodes in each direction. Equations (11) and (14) are approximated spatially using central differences [5, 26] leading to the following second-order accurate spatial discretizations:

$$\frac{\partial h_{i,j}}{\partial t} = \frac{1}{\Delta^2}\left[\left.\frac{h^3}{3}\right|_{i+(1/2),j}(p_{i+1,j} - p_{i,j}) - \left.\frac{h^3}{3}\right|_{i-(1/2),j}(p_{i,j} - p_{i-1,j}) + \left.\frac{h^3}{3}\right|_{i,j+(1/2)}(p_{i,j+1} - p_{i,j}) - \left.\frac{h^3}{3}\right|_{i,j-(1/2)}(p_{i,j} - p_{i,j-1})\right] - \frac{B_o}{\varepsilon}\sin\alpha h_{i,j}^2\left(\frac{h_{i+1,j} - h_{i-1,j}}{2\Delta}\right) + O(\Delta^2) \tag{16}$$

$$p_{i,j} + \frac{1}{\Delta^2}[(h_{i+1,j} + s_{i+1,j}) + (h_{i-1,j} + s_{i-1,j}) + (h_{i,j+1} + s_{i,j+1}) + (h_{i,j-1} + s_{i,j-1}) - 4(h_{i,j} + s_{i,j})] + \frac{(n-1)(m-1)(1-\cos\Theta_e)}{h^*(n-m)\varepsilon^2} \times \left[\left(\frac{h^*}{h_{i,j}}\right)^n - \left(\frac{h^*}{h_{i,j}}\right)^m\right] - B_o(h_{i,j} + s_{i,j})\cos\alpha + O(\Delta^2) = 0 \tag{17}$$

for each (i, j) in the computational domain, where Δ is the spatial increment ($\Delta = 2^{-k_f}$ for the finest grid level) and the $h^3/3|_{i\pm(1/2),j}$, $h^3/3|_{i,j\pm(1/2)}$ terms are the *pre-factors* associated with the discretization. Here results are obtained using Zhornitskaya and Bertozzi's [23] *Positivity Preserving Scheme* for which the pre-factors in Equation (16) can be shown to be given by

$$\left.\frac{h^3}{3}\right|_{i+(1/2),j} = \frac{2}{3}\frac{h_{i,j}^2 h_{i+1,j}^2}{h_{i+1,j} + h_{i,j}} \tag{18}$$

with similar expressions for the $h^3/3|_{i-(1/2),j}$, $h^3/3|_{i,j+(1/2)}$ and $h^3/3|_{i,j-(1/2)}$ terms.

3.2. Temporal discretization

Ideally, time-stepping schemes for the numerical solution of transient flows should be both *efficient* and *accurate*. The former ensures that small time steps are avoided when the solution varies slowly while the latter should enable the error to be controlled throughout the solution process. Most previous numerical studies of lubrication-type flows have focussed on increasing the efficiency of the solution and, in particular, overcoming the stability requirement for explicit schemes that the time step Δt should be $O(\Delta^4)$—an impractical restriction when even moderate spatial resolution is employed. Several studies have achieved this using alternating-direction implicit (ADI) algorithms employing alternate sweeps in each direction so that only a banded system of equations need be solved at each time step [5]. These *time-splitting* algorithms enable time steps several orders of magnitude larger than $O(\Delta^4)$ to be used successfully.

Few studies have reported attempts to control the accuracy of time-stepping schemes and it is only very recently that an estimate of the local truncation error has been used when solving equations of the form (11) and (14) to test whether they are being solved to a specified error tolerance [26]. The latter's scheme, however, does not optimize the time step for a given error tolerance. The present work addresses this issue by using time-stepping based on local error estimates from an implicit, second-order method which reduces to Heun's method [19] in the case of a fixed time step. This uses an estimate of the local truncation error, obtained from the difference between this solution and an explicit predictor, to increase the time step in a controlled manner whilst at the same time minimizing the computational expense associated with repeated time step failure.

This approach requires Equation (16) to be rewritten as a system of differential–algebraic equations in the form

$$\frac{\partial h_{i,j}}{\partial t} = F(h_{i,j}, p_{i,j}, h_{i\pm1,j}, p_{i\pm1,j}, h_{i,j\pm1}, p_{i,j\pm1}) \tag{19}$$

for each (i,j) in the computational domain. The predictor stage is fully explicit, second-order accurate in time and proceeds by solving

$$h^{n+1}_{i,j_{\text{Predict}}} = \beta^2 h^{n-1}_{i,j} + (1-\beta^2)h^n_{i,j} + \Delta t^{n+1}(1+\beta)F(h^n_{i,j}, p^n_{i,j}, h^n_{i\pm1,j}, p^n_{i\pm1,j}, h^n_{i,j\pm1}, p^n_{i,j\pm1}) \tag{20}$$

where $\beta = \Delta t^{n+1}/\Delta t^n$ and the superscript n denotes data at the nth time step. It can be shown, via a Taylor series expansion of Equation (20), that the local truncation error (LTE) for the predictor stage is given by

$$(\text{LTE}_{\text{Predict}})_{i,j} = \left.\frac{(\Delta t^{n+1})^2 \Delta t^n (1+\beta)}{6}\,\frac{\partial^3 h_{i,j}}{\partial t^3}\right|_{t=t_p} \tag{21}$$

where the third derivative term is evaluated at a time $t_p \in (t_n, t_{n+1})$.

The solution stage is implicit and is also second-order accurate in time, given by

$$\begin{aligned} h^{n+1}_{i,j} - \frac{\Delta t^{n+1}}{2} F(h^{n+1}_{i,j}, p^{n+1}_{i,j}, h^{n+1}_{i\pm1,j}, p^{n+1}_{i\pm1,j}, h^{n+1}_{i,j\pm1}, p^{n+1}_{i,j\pm1}) \\ = h^n_{i,j} + \frac{\Delta t^{n+1}}{2} F(h^n_{i,j}, p^n_{i,j}, h^n_{i\pm1,j}, p^n_{i\pm1,j}, h^n_{i,j\pm1}, p^n_{i,j\pm1}) \end{aligned} \tag{22}$$

for which the LTE is

$$(\text{LTE})_{i,j} = \frac{-1}{12}(\Delta t_{n+1})^3 \left.\frac{\partial^3 h_{i,j}}{\partial t^3}\right|_{t=t_c}, \quad t_c \in (t_n, t_{n+1}) \tag{23}$$

As described in Reference [19], the assumption that the third-order derivative term varies only a small amount over the time step enables the LTE to be estimated by

$$(\text{LTE})_{i,j} = \frac{1}{1+2((1+\beta)/\beta)}(h^{n+1}_{i,j} - h^{n+1}_{i,j_{\text{Predict}}}) \tag{24}$$

Following Reference [27], this expression is used to obtain an estimate of the overall truncation error by finding its Euclidean norm, $\|\text{LTE}\|$, which is then used to specify the next time step

throughout the domain, Δt^{n+2}, via

$$\Delta t^{n+2} = 0.9\Delta t^{n+1}\left(\frac{\mathrm{TOL}}{\|\mathrm{LTE}\|}\right)^{1/3} \tag{25}$$

if $\|\mathrm{LTE}\| \leqslant \mathrm{TOL}$, whereas if $\|\mathrm{LTE}\| > \mathrm{TOL}$ the iteration is restarted with half the current time step.

The implicit system of algebraic equations (17) and (22) are solved at each time step using the FAS multigrid method described below.

3.3. The multigrid solver

There is much in the literature surrounding multigrid methods (e.g. References [13–18]), suffice it to say that they are fast solvers, the essence of which is to use a simple iterative technique as a smoother, not as a solver, to reduce high frequency errors on the computational grid while lower frequency errors are smoothed out on a succession of coarser computational grids. A hierarchy of grids is defined, $G^0, G^1, \ldots, G^L$ say, where the grid spacing halves from one grid to the next and where G^0 denotes the coarsest grid and G^L the finest. Note that, for all solutions presented later the coarsest grid level G^0 is a 17×17 one so that the finest grid level G^L, i.e. the one on which the solution is actually sought, has $2^{L+4}+1$ nodes in either direction or, in terms of the fine grid parameter introduced above, $k_f = L+4$. Multigrid solutions are reported where the finest grid level ranges from G^2 with 65×65 nodes to G^6 with 1025×1025 nodes. For example, if a multigrid solution is desired on a 129×129 grid then this corresponds to grid G^3 with intermediate solutions obtained on grids G^0 (17×17), G^1 (33×33) and G^2 (65×65) before the final solution on G^3 is actually obtained. Note that the grid spacing associated with each grid level G^k is uniform and equal in both directions and simply $\Delta^k = 1/(2^{k+4})$.

The non-linear discretized Equations (17) and (22) are solved using a combination of the full approximation storage (FAS) method and full multigrid technique [13–18]. Figure 2

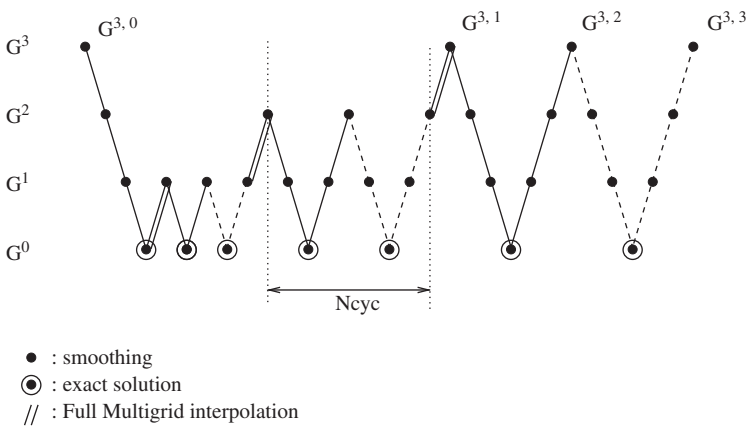

Figure 2. Description of the full multigrid technique when solutions are obtained on grid G^3 with 129 nodes in either direction. $G^{3,0}$ represents the initial solution on G^3 at the previous time step, $G^{3,1}$ the solution after the first fine grid V-cycle, $G^{3,2}$ the solution after two V-cycles, etc.

illustrates the structure of the solution process over the four grid levels that are used when a solution on, say, grid level G^3, i.e. 129×129, is obtained. An important advantage of this technique is that an initial guess to the solution at a given level is provided by the interpolation of the solution on the next coarsest level. At all but the coarsest grid level a fixed number of V-cycles are applied, the same number of V-cycles, N_{cyc}, being applied at all intermediate grid levels G^k for which $0 < k < L$. At the coarsest level an exact non-linear solver may be applied or a large number of smoothing iterations performed: in this work the former approach is adopted, based upon Newton's method. At the very beginning of the full multigrid cycle the solution from the previous time step is used to provide an initial residual and as a starting point for the multigrid procedure.

In order to explain clearly the steps taken during a single V-cycle, the governing equations (17) and (22), at the particular grid level k, may be rewritten in the following way:

$$\mathscr{L}_k^p(\underline{h}_k^{n+1}, \underline{p}_k^{n+1}) = 0 \tag{26}$$

$$\mathscr{L}_k^h(\underline{h}_k^{n+1}, \underline{p}_k^{n+1}) = f_k^h(\underline{h}_k^n, \underline{p}_k^n) \tag{27}$$

where the film thicknesses and pressure at the nth time step t_n are known and are given by $\underline{h}_k^n = \{h_{ij_k}^n\}$ and $\underline{p}_k^n = \{p_{ij_k}^n\}$, and f_k^h corresponds to the right-hand side of Equation (22).

Given $\underline{h}_{0_k}^{n+1}$ and $\underline{p}_{0_k}^{n+1}$ as an initial guess to the solution of Equations (26) and (27), the computed values after completion of the V-cycle are: $\underline{h}_{1_k}^{n+1}$ and $\underline{p}_{1_k}^{n+1}$. Each V-cycle within the solution process may be defined in a recursive way using precisely the same pseudo-code formalism as in Trottenberg [28]: In functional notation this V-cycle from level k may be written as

$$(\underline{h}_{1_k}^{n+1}, \underline{p}_{1_k}^{n+1}) = \text{FASCYC}(k, \underline{h}_{0_k}^{n+1}, \underline{p}_{0_k}^{n+1}, f_k^h, f_k^p, n_{\text{pre}}, n_{\text{post}})$$

The function FASCYC may be broken down into three distinct stages:

1. *Presmoothing stage*:
   - Apply n_{pre} times a red–black Gauss–Seidel scheme [29] to a linearized form of Equations (26) and (27) so that, in functional notation:

$$(\underline{\tilde{h}}_{0_k}^{n+1}, \underline{\tilde{p}}_{0_k}^{n+1}) = \text{RELAX}^{n\text{pre}}(\underline{h}_{0_k}^{n+1}, \underline{p}_{0_k}^{n+1}, f_k^h, f_k^p)$$

2. *Coarse grid correction stage*:
   - Compute the defects:

$$d_k^h = f_k^h - \mathscr{L}_k^h(\underline{\tilde{h}}_{0_k}^{n+1}, \underline{\tilde{p}}_{0_k}^{n+1}), \quad d_k^p = f_k^p - \mathscr{L}_k^p(\underline{\tilde{h}}_{0_k}^{n+1}, \underline{\tilde{p}}_{0_k}^{n+1})$$

     (Note that in our case, from Equation (26), $f_L^p = 0$, however this is not the case in general for $k < L$, as shown below.)
   - Restrict the defect to the next coarse grid level using a half-weighting restriction operator, R_k^{k-1} [13]:

$$d_{k-1}^h = R_k^{k-1}(d_k^h), \quad d_{k-1}^p = R_k^{k-1}(d_k^p)$$

- Restrict $\underline{\tilde{h}_0}_k^{n+1}$ and $\underline{\tilde{p}_0}_k^{n+1}$ in the same way:

$$\underline{\tilde{h}_0}_{k-1}^{n+1} = R_k^{k-1}(\underline{\tilde{h}_0}_k^{n+1}), \quad \underline{\tilde{p}_0}_{k-1}^{n+1} = R_k^{k-1}(\underline{\tilde{p}_0}_k^{n+1})$$

- Compute the right-hand side at the next coarser level:

$$f_{k-1}^h = d_{k-1}^h + \mathscr{L}_{k-1}^h(\underline{\tilde{h}_0}_{k-1}^{n+1}, \underline{\tilde{p}_0}_{k-1}^{n+1}), \quad f_{k-1}^p = d_{k-1}^p + \mathscr{L}_{k-1}^p(\underline{\tilde{h}_0}_{k-1}^{n+1}, \underline{\tilde{p}_0}_{k-1}^{n+1})$$

- Compute an approximate solution $\underline{\hat{w}}_{k-1}^h, \underline{\hat{w}}_{k-1}^p$ of the coarse grid equation on G^{k-1}:

$$\mathscr{L}_{k-1}^h(\underline{w}_{k-1}^h, \underline{w}_{k-1}^p) = f_{k-1}^h \tag{28}$$

$$\mathscr{L}_{k-1}^p(\underline{w}_{k-1}^h, \underline{w}_{k-1}^p) = f_{k-1}^p \tag{29}$$

  If $k = 1$: find the exact solution using the coarse grid solver.
  If $k > 1$: solve Equations (28) and (29) by performing the FAS cycle using $\underline{\tilde{h}_0}_{k-1}^{n+1}$ and $\underline{\tilde{p}_0}_{k-1}^{n+1}$ as an initial approximation:

$$(\underline{\hat{w}}_{k-1}^h, \underline{\hat{w}}_{k-1}^p) = \mathrm{FASCYC}(k-1, \underline{\tilde{h}_0}_{k-1}^{n+1}, \underline{\tilde{p}_0}_{k-1}^{n+1}, f_{k-1}^h, f_{k-1}^p, n_{\mathrm{pre}}, n_{\mathrm{post}})$$

- Compute the corrections:

$$\underline{\hat{v}}_{k-1}^h = \underline{\hat{w}}_{k-1}^h - \underline{\tilde{h}_0}_{k-1}^{n+1}, \quad \underline{\hat{v}}_{k-1}^p = \underline{\hat{w}}_{k-1}^p - \underline{\tilde{p}_0}_{k-1}^{n+1}$$

- Interpolate the corrections using the bilinear interpolation operator, I_{k-1}^k [13]:

$$\underline{\hat{v}}_k^h = I_{k-1}^k(\underline{\hat{v}}_{k-1}^h), \quad \underline{\hat{v}}_k^p = I_{k-1}^k(\underline{\hat{v}}_{k-1}^p)$$

- Compute the corrected approximation on G^k:

$$\underline{h_0}_k^{n+1} = \underline{\tilde{h}_0}_k^{n+1} + \underline{\hat{v}}_k^h, \quad \underline{p_0}_k^{n+1} = \underline{\tilde{p}_0}_k^{n+1} + \underline{\hat{v}}_k^p$$

3. *Postsmoothing stage*:
   - Apply n_{post} times the relaxation scheme:

$$(\underline{h_1}_k^{n+1}, \underline{p_1}_k^{n+1}) = \mathrm{RELAX}^{n\mathrm{post}}(\underline{h_0}_k^{n+1}, \underline{p_0}_k^{n+1}, f_k^h, f_k^p)$$

The associated relaxation scheme consists of a single Newton iteration solved with a fixed number of sweeps (n_{pre} or n_{post}) of Red–Black Gauss–Seidel. The linearized form of equations (26) and (27) is obtained by computing the local Jacobian only, so that each relaxation sweep (in the pre-smooth stage for example) proceeds by solving:

$$\frac{\partial \mathscr{L}_k^h}{\partial h_{ij_k}^{n+1}} \Delta h + \frac{\partial \mathscr{L}_k^h}{\partial p_{ij_k}^{n+1}} \Delta p = f_k^h - \mathscr{L}_k^h(\underline{h_0}_k^{n+1}, \underline{p_0}_k^{n+1}) \tag{30}$$

$$\frac{\partial \mathscr{L}_k^p}{\partial h_{ij_k}^{n+1}} \Delta h + \frac{\partial \mathscr{L}_k^p}{\partial p_{ij_k}^{n+1}} \Delta p = f_k^p - \mathscr{L}_k^p(\underline{h_0}_k^{n+1}, \underline{p_0}_k^{n+1}) \tag{31}$$

for Δh and Δp. Hence a new approximation to the solution is given by: $\widetilde{h_{0i,j_k}}^{n+1} = h_{0i,j_k}^{n+1} + \Delta h$, $\widetilde{p_{0i,j_k}}^{n+1} = p_{0i,j_k}^{n+1} + \Delta p$. The Neumann boundary conditions are treated by introducing ghost nodes outside the computational domain and by imposing the values of droplet thicknesses and pressure at these points to be the same values as those at the boundary.

At the coarsest level (G^0), the discretized equations are solved using a Newton iteration scheme. The iteration is defined in terms of the Jacobian matrices:

$$\underline{\underline{A}} = \frac{\partial \mathscr{L}_0^p}{\partial \underline{p}_0^{n+1}}, \quad \underline{\underline{B}} = \frac{\partial \mathscr{L}_0^p}{\partial \underline{h}_0^{n+1}}, \quad \underline{\underline{C}} = \frac{\partial \mathscr{L}_0^h}{\partial \underline{p}_0^{n+1}}, \quad \underline{\underline{D}} = \frac{\partial \mathscr{L}_0^h}{\partial \underline{h}_0^{n+1}} \tag{32}$$

Given $\underline{w}_0^h, \underline{w}_0^p$ as first approximations to the solution of the coarse grid Equations (28) and (29), then increments to $\underline{w}_0^h, \underline{w}_0^p$, $\underline{\Delta w}_0^h$ and $\underline{\Delta w}_0^p$, respectively, are obtained by solving the linearized Newton iteration equations:

$$\underline{\underline{A}}\,\underline{\Delta w}_0^p + \underline{\underline{B}}\,\underline{\Delta w}_0^h = f_0^p - \mathscr{L}_0^p(\underline{w}_0^h, \underline{w}_0^p) \tag{33}$$

$$\underline{\underline{C}}\,\underline{\Delta w}_0^p + \underline{\underline{D}}\,\underline{\Delta w}_0^h = f_0^h - \mathscr{L}_0^h(\underline{w}_0^h, \underline{w}_0^p) \tag{34}$$

Solution of these equations is obtained as follows. Setting $\underline{\Delta w}_0^h = \underline{0}$ in (33), an initial approximation to $\underline{\Delta w}_0^p$ is: $\underline{\Delta w}_0^{p'} = \underline{\underline{A}}^{-1}(f_0^p - \mathscr{L}_0^p(\underline{w}_0^h, \underline{w}_0^p))$, while the equation for $\underline{\Delta w}_0^h$ is obtained by eliminating $\underline{\Delta w}_0^p$ from Equations (33) and (34), viz.

$$(\underline{\underline{D}} - \underline{\underline{C}}\,\underline{\underline{A}}^{-1}\underline{\underline{B}})\underline{\Delta w}_0^h = f_0^h - \mathscr{L}_0^h(\underline{w}_0^h, \underline{w}_0^p) - \underline{\underline{C}}\,\underline{\Delta w}_0^{p'} \tag{35}$$

Equation (35) is solved to yield $\underline{\Delta w}_0^h$ and $\underline{w}_0^h, \underline{w}_0^p$ are updated according to $\underline{w}_0^h \to \underline{w}_0^h + \underline{\Delta w}_0^h$ and $\underline{w}_0^p \to \underline{w}_0^p + \underline{\Delta w}_0^{p'} - \underline{\underline{A}}^{-1}\underline{\underline{B}}\underline{\Delta w}_0^h$, respectively. The iteration proceeds until the norm

$$\frac{\sqrt{|f_0^p - \mathscr{L}_0^p(\underline{w}_0^h, \underline{w}_0^p)|^2 + |f_0^h - \mathscr{L}_0^h(\underline{w}_0^h, \underline{w}_0^p)|^2}}{n}$$

where n is the number of unknowns in one direction, is sufficiently small. In this work we found that a relative reduction in the residual of just 10^{-3} (compared to the initial residual from the solution at the previous time step) to be sufficient, however much greater accuracies are easily obtainable if required.

4. RESULTS

The efficiency and accuracy of the multigrid method is first demonstrated by comparison with a series of analytical and previously reported numerical results for droplet spreading flows. New results are then presented which show how the method can be readily applied to simulate droplet motion on substrates with topographic and/or wettability inhomogeneities.

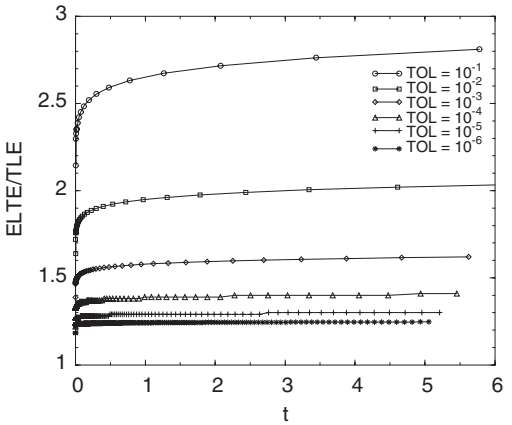

Figure 3. Ratio of ELTE to TLE for Equation (36) as a function of time, t, and TOL.

4.1. *Accuracy of the local error estimate*

The accuracy of the estimate of LTE, Equation (24), is demonstrated by comparing it with the true local error for the ordinary differential equation

$$\frac{\mathrm{d}h}{\mathrm{d}t} + \frac{1}{5}\frac{h}{t} = 0, \quad h(t_0) = h_0 \tag{36}$$

This equation is chosen since its analytical solution

$$h(t) = h_0 \left(\frac{t_0}{t}\right)^{0.2} \tag{37}$$

is of exactly the same form as Tanner's [30] closed form solution for film thickness at the centre of an axisymmetrically spreading droplet over a homogeneous substrate—see later. If h_n is the numerical solution of Equation (36) obtained at time t_n using the temporal discretization scheme described above, then the true local error is the difference between h_{n+1}, the numerical solution obtained at time t_{n+1}, and the corresponding analytical solution for the same initial condition $h(t_n) = h_n$, namely $h_n(t_n/t_{n+1})^{0.2}$.

Figure 3 shows how the ratio of the estimated local truncation error, ELTE, (24) to the true local error, TLE, varies with time and prescribed error tolerance, TOL. It demonstrates that the estimate consistently over predicts the true error and that decreasing the tolerance increases the accuracy of the estimate to the extent that for $\mathrm{TOL} < 10^{-4}$ the estimated local error is within 30% of its true value.

4.2. *Efficiency of the numerical method*

The efficiency of the multigrid and time-stepping procedures are demonstrated by considering the problem of droplet spreading on a horizontal substrate for a partially wetting system where the equilibrium contact angle ($\Theta_e > 0$) and the effects of gravity are neglected

($B_o = 0$). For the particular case of a spreading axisymmetric droplet, centred initially at $(x, y) = (0.5, 0.5)$, the film thickness at the droplet centre, $h_0(t)$, is given [30] by

$$h_0(t) = \frac{K}{t^\beta} \quad \text{for } t > 0 \tag{38}$$

where K and β ($= 0.2$) are spreading constants, a result verified by Lelah and Marmur's [31] experiments which found $0.16 \leqslant \beta \leqslant 0.32$. The axisymmetric lubrication equations for this problem were subsequently solved numerically by Schwartz and Eley [8] who investigated the influence of the precursor film thickness h^* on the spreading rate parameters K and β in Equation (38). Here, this flow is studied by solving the lubrication equations (11) and (14) for particular case of $\varepsilon = 0.005$, $(n, m) = (3, 2)$, the initial droplet profile is given by

$$h(r) = \max\left(5\left(1 - \frac{320}{9}r^2\right), h^*\right) \tag{39}$$

where r is the radius of the footprint of the droplet on the surface of the substrate. An equilibrium contact angle of 1.53° was chosen so that $h_0(t) \to 1$ at large times. Note that, apart from the initial profile no axisymmetry is imposed in the numerical solutions.

The following sequence of figures elucidate the effect of the multigrid parameters on the convergence of solutions by plotting the relative residuals at the finest grid level, which are defined as the ratio of the residual at the finest grid level after a given number of fine grid V-cycles compared to the initial residual at the beginning of the time step.

The effect of the number of V-cycles (N_{cyc}) at intermediate grid levels ($0 < k < L$) on the relative residuals, where the finest grid level is 129×129 (i.e. $L = 3$) and the fixed (for this comparison) time step is 10^{-9}, is shown in Figure 4(a). It clearly demonstrates the benefit of using at least one V-cycle at the intermediate level as the relative residuals are reduced by almost two orders of magnitude compared to the case where no intermediate V-cycle is used. Although more than one V-cycle does not improve noticeably the convergence of the solution at the finest level but using a higher order interpolation scheme such as bicubic interpolation for the Full Multigrid interpolation instead of bilinear interpolation may increase the benefit of using more intermediate V-cycles. The initial increase in relative residuals is due to the fact that at the beginning of the solution process the initial guess, which corresponds to the solution at the previous time step, satisfies (26) exactly since its right-hand side does not change. Thus, after a first cycle, despite a reduction of the residuals for Equation (27), the residuals of Equation (26) can only increase. The magnitude of this initial increase in relative residuals is critical to the success of the solution procedure and therefore, a larger number of presmoothing sweeps is performed for the first V-Cycle ($n_{\text{pre}} = 4$) while two presmoothing sweeps only are found to be sufficient for the following V-cycles: n_{post} is set to 2 regardless of the cycle number.

The effect of the grid size at the finest level is explored next for a fixed number of intermediate V-cycles ($N_{\text{cyc}} = 3$) and $\Delta t^{n+1} = 10^{-9}$. Figure 4(b) shows that for all grids, with L ranging from 3 (129×129) to 5 (513×513), the ratio of the residuals after the completion of the V-cycle is effectively independent of the finest grid level. Closer analysis of the data reveals that this ratio takes a value of approximately 1/20. Figure 4(c) shows that (fixed) time step size has little effect on the convergence history until a threshold value $\Delta t_{\max} = 5 \times 10^{-8}$ is reached. The initial increase in relative residuals becomes steeper and above this threshold value the solution procedure fails. This limiting value of the time step depends on both the

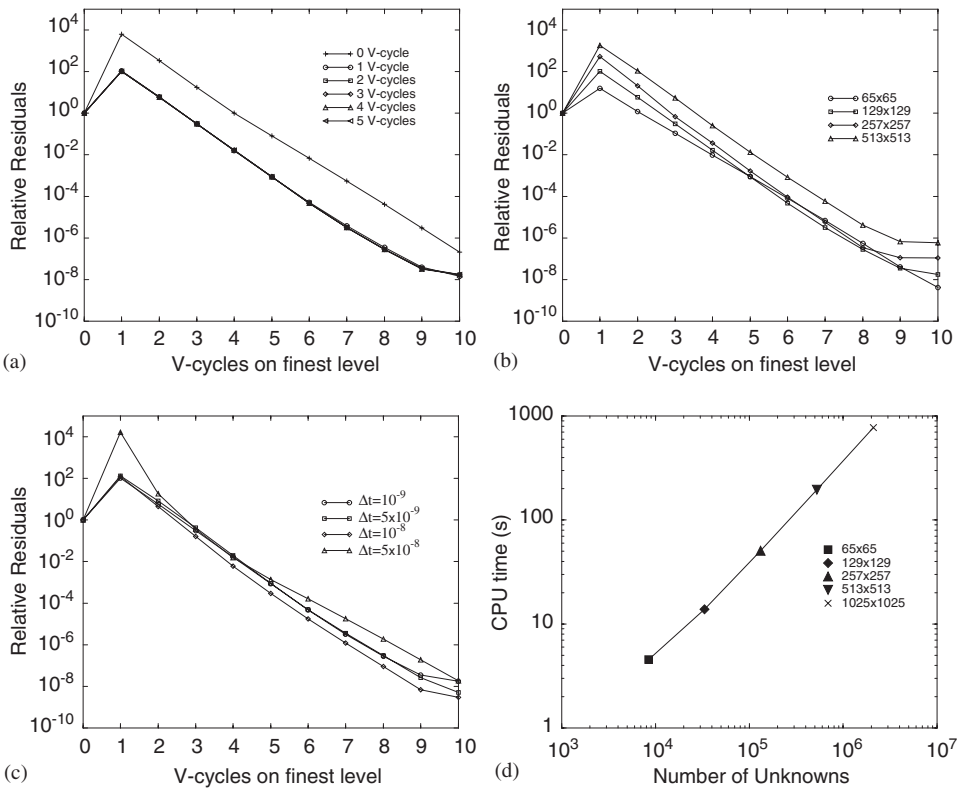

Figure 4. Effect of multigrid parameters on the convergence history of solutions. (a) Effect of the number of V-cycles (N_{cyc}) at the intermediate grid levels on the convergence history of solutions. The finest grid level, G^3, is 129×129 and $\Delta t^{n+1} = 10^{-9}$. (b) Effect of the finest grid level on the convergence history of solutions with $N_{\text{cyc}} = 3$ and $\Delta t^{n+3} = 10^{-9}$. (c) Effect of time step on the convergence history of solutions with $N_{\text{cyc}} = 3$ and the finest grid level, G^3, is 129×129. (d): Dependence of CPU time for a typical time step as a function of the total number of unknowns. Flow conditions: evolution of a partially wetting droplet with $B_o = 0$, $\varepsilon = 0.005$, $\Theta_e = 1.53^\circ$, $h^* = 0.04$ and $(n, m) = (3, 2)$, $\text{TOL} = 10^{-4}$.

mesh size and how advanced the solution is: as finer and finer grids are used, $\Delta t_{\max}$ decreases and at later times, $\Delta t_{\max}$ increases. Note that the calculations are for very early times where the spreading motion is most active and the demands on the multigrid solver are most severe. An additional advantage therefore of the adaptive time-stepping scheme described previously is that the time-step selected is always smaller than this limiting time step as no restart of the solution procedure is ever necessary.

In light of the above, all subsequent results were obtained using five V-cycles at each level. Although clearly over-cautious, this has only a small additional computational cost since most of the computational time is spent performing cycles at the finest level.

Figure 4(d) shows how the CPU time for a typical time step depends on grid density and demonstrates that one of the most important potential advantages of Multigrid methods,

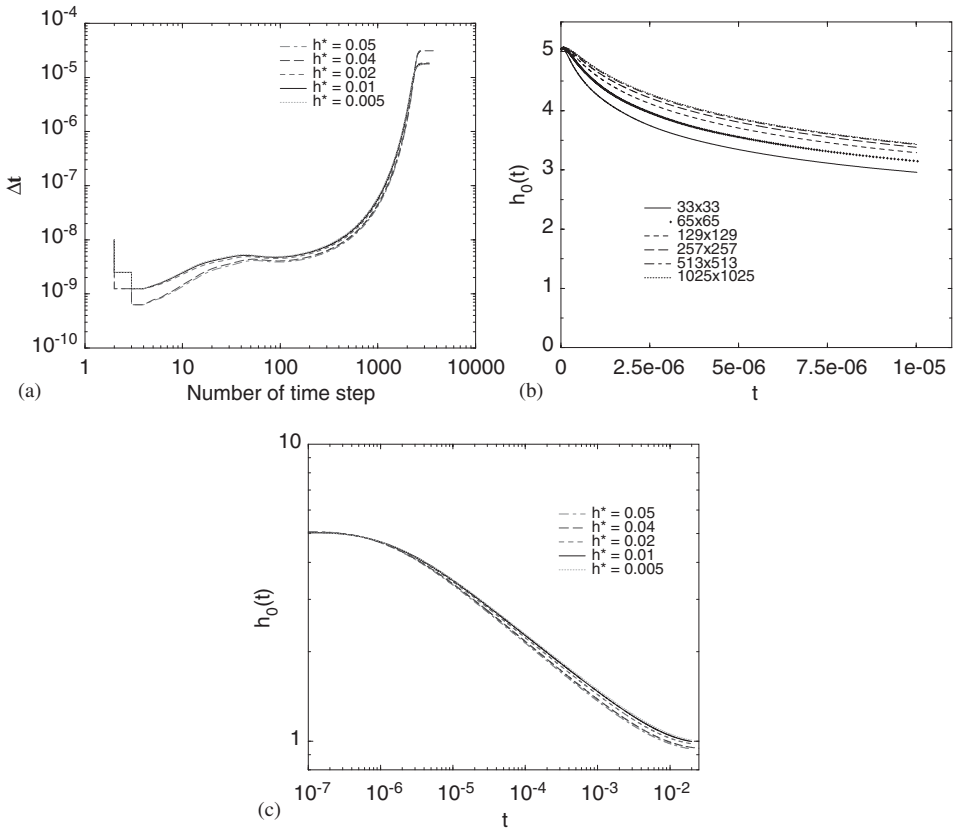

Figure 5. (a) Effect of precursor film thickness h^* on time step evolution. The finest grid level is G^4, i.e. 257×257. (b) Multigrid solutions of the droplet thickness at the centre of a partially wetting droplet as a function of time, t, and grid density with $h^* = 0.04$. (c) Multigrid solutions of the droplet thickness at the centre of a partially wetting droplet as a function of time, t, and precursor film thickness h^*. The finest grid level is G^4, i.e. 257×257. Simulation parameters: $B_o = 0$, $\varepsilon = 0.005$, $(n, m) = (3, 2)$, $\Theta_e = 1.53^\circ$ and $\mathrm{TOL} = 10^{-4}$.

namely that CPU time varies linearly (i.e. the slope of the line in Figure 4(d) ≈ 1) with the total number of unknowns, is achieved by the solver. As noted above, when allied to ever-increasing computational power, this feature of the solver is particularly important when small-scale phenomena need to be simulated efficiently and accurately.

Figure 5(a) illustrates how the time step varies as a function of h^*, showing that after the solution has settled down the time-stepping scheme enables substantial efficiency gains to be realized at later times and that the value of h^* has only a marginal influence in the sense that the larger h^* values permit larger time steps to be used near the equilibrium state.

The accuracy of the solutions is considered next. Figure 5(b) investigates the effect of grid size on the droplet thickness $h_0(t)$ for simulations where $h^* = 0.04$ and $\mathrm{TOL} = 1 \times 10^{-4}$.

Table I. The effect of precursor film thickness h^* on spreading rate parameters: finest grid level is 257×257, with $\mathrm{TOL} = 10^{-4}$.

h^*	K	β	Rescaled K
0.05	0.353	0.196	0.615
0.04	0.362	0.194	0.627
0.02	0.385	0.191	0.661
0.01	0.407	0.187	0.691
0.005	0.41	0.187	0.696

It shows that the solution converges with respect to the spatial discretization as the grid is progressively refined and that the solutions on the three finest grid levels differ by only approximately 1%. The influence of the precursor film thickness h^* is shown in Figure 5(c), for solutions obtained with a finest grid level of 257×257, $\mathrm{TOL} = 10^{-4}$ and adaptive time stepping. It illustrates that after an initial phase the droplet thickness $h_0(t)$ obeys the expected power law relationship $h_0(t) = K/t^{\beta}$, where the coefficients K and β are shown in Table I. Note that, owing to the time scaling employed in the present study, in order to compare these results with those of Schwartz and Eley [8] the K values must be multiplied by the factor $0.059^{-\beta}$. The β values are found to be close to the expected value of 0.2, [30], and the values of K also compare well with the values $K = 0.61$ ($h^* = 0.05$) and 0.68 ($h^* = 0.005$) obtained by Reference [8].

4.3. Large bond number spreading of an axisymmetric droplet

Comparison is made between numerical predictions and corresponding analytical solutions for the case of axisymmetric spreading flow of a completely wetting droplet, centred initially at $(x, y) = (0.5, 0.5)$, over a horizontal substrate when gravitational effects dominate over surface tension ones so that the Bond number, B_o, is large. In this case the lubrication equations for the droplet thickness h can be reduced to the following second-order p.d.e. for axisymmetric flow

$$\frac{\partial h}{\partial t} = \frac{B_o}{3r} \frac{\partial}{\partial r} \left[r h^3 \frac{\partial h}{\partial r} \right] \tag{40}$$

in terms of r, the radial distance from the centre of the substrate.

The idealized case where the initial droplet profile is in the form of a Dirac delta function, given by

$$h(r, t = 0) = 0 \text{ for } r > 0 \quad \text{and} \quad 2\pi \int_0^{\infty} rh \, \mathrm{d}r = V \tag{41}$$

where V is the dimensionless volume of the droplet, has been analysed previously in [32]. The latter study showed that Equation (40) could be solved analytically by defining the similarity variable $\xi = r(3/B_o V^3 t)^{1/8}$, to yield

$$h(\xi) = 0.753 \left(\frac{V}{tB_o} \right)^{1/4} (0.799 - \xi^2)^{1/3} \tag{42}$$

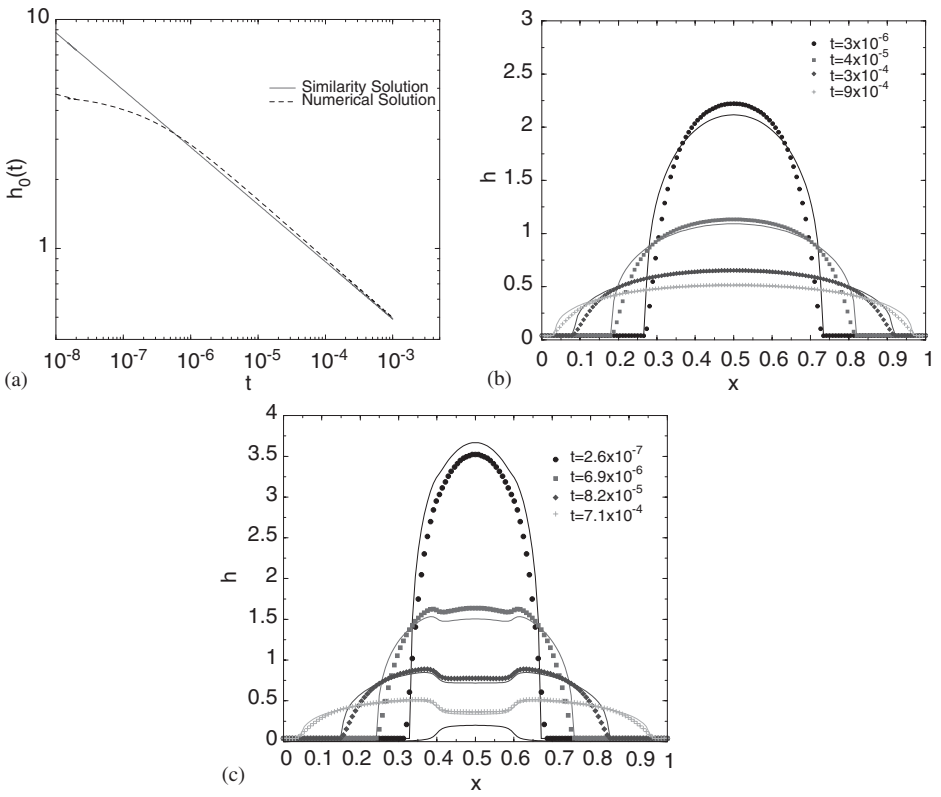

Figure 6. (a) Droplet thickness at the centre of a completely wetting droplet $h_0(t)$: comparison between the numerical predictions and the similarity solution (42). (b) Cross-sectional thickness profiles across a completely wetting droplet: comparison between numerical predictions (symbols) and the similarity solution (42). (c) Cross-sectional thickness (h) profiles for a completely wetting droplet over a circular topography: comparison between numerical predictions (symbols) and the similarity solution (44). Simulation parameters: $B_o = 1066$, $V = 0.261$, finest grid level equals 129×129 and $\mathrm{TOL} = 2.5 \times 10^{-3}$.

Figure 6(a) compares numerical predictions of the droplet thickness at its centre, $h_0(t)$, as a function of time with the similarity solution (42) for the case $B_o = 1066$ and $V = 0.261$. The former are obtained with a finest grid level of 129×129 and $\mathrm{TOL} = 2.5 \times 10^{-3}$. The simulation uses the initial profile (39) since it is both sharply peaked and mimics, to some extent, the initial conditions in the analytical solution whilst at the same time guaranteeing that $h_0(t)$ changes substantially before the droplet flows out of the computational domain $\left(0 \leqslant r \leqslant \sqrt{2}/2\right)$.

As expected, the agreement between the simulation and similarity solution is initially poor (for $t < 3 \times 10^{-7}$), due to the differences between the initial conditions in the two solutions, but improves at later times and eventually becomes very good beyond this initial phase where the maximum film thickness $h_0(t)$ decreases in proportion to $t^{-1/4}$ at later times. Similar agreement is also seen in Figure 6(b), which shows the development of the thickness profile across the droplet, where the agreement at later times is very good everywhere except near the

contact line. The latter discrepancies are caused by the small, but non-zero, surface tension in the simulations which acts to reduce curvature in its vicinity.

4.4. New results for droplet spreading over topographies

The remaining results concern examples of the flow of droplets over topographic features. Consider first the previous problem of axisymmetric flow of a completely wetting droplet at high Bond number extended to the case of a completely enveloped circular topography. It can be shown that the similarity solution (42) for the flow in the absence of a topography is only slightly modified by its presence since the governing equation (40) simply becomes

$$\frac{\partial h}{\partial t} = \frac{B_o}{3r}\frac{\partial}{\partial r}\left[rh^3\frac{\partial(h+s)}{\partial r}\right] \tag{43}$$

where $s = s(r)$ is the topographic profile. Since $s(r)$ does not vary with time it is easy to show that the similarity solution with a topography is given by

$$h(\xi) = 0.753\left(\frac{V}{t\,B_o}\right)^{1/4}(0.799 - \xi^2)^{1/3} - s(r) \tag{44}$$

where, once again, $\xi = r(3/B_o V^3 t)^{1/8}$.

The topography $s(r)$ is given by

$$s(r) = s_0\left(\frac{T(r) - T\left(\sqrt{2}/2\right)}{T(0) - T\left(\sqrt{2}/2\right)}\right) \tag{45}$$

where s_0 is its height and, following Reference [33], $T(r)$ is an arctangent function

$$T(r) = \tan^{-1}\left(\frac{\pi}{2\gamma}\left(1 - \frac{r}{r_t}\right)\right) \tag{46}$$

where the parameter γ controls the steepness of the topography and $r_t = R_t/L_0$ is its radius.

Figure 6(c) shows a comparison between numerical predictions of the droplet thickness (h) profile across the film and the similarity solution (44) for the particular case of a topography with $s_0 = 0.2$, $\gamma = 0.2$ and $r_t = 0.1$, the former having been obtained with a finest grid level of 129×129 and $\mathrm{TOL} = 2.5 \times 10^{-3}$. As in the related case without a topography, results are obtained for $B_o = 1066$ and $V = 0.261$, while the droplet thickness profile (39) is modified so that the initial free surface profile is the same in both cases, i.e.

$$h + s = \max\left(5\left(1 - \frac{320}{9}r^2\right), s(r) + h^*\right) \tag{47}$$

The figure shows similar behaviour to that reported in Figure 6(b) for the case without a topography.

Next droplet spreading over substrates containing three-dimensional, rectangular topographies is explored. The extent of the topography is specified with respect to the reference point $(x_1, y_1) = (X_1, Y_1)/L_0$ as indicated in Figure 1. Following Reference [2] the topography

$s(x, y)$ is defined in terms of transformed co-ordinates, (x^*, y^*) say, with origin at the centre of the topography and given by

$$x^* = x - x_1 - 0.5l_t; \quad y^* = y - y_1 - 0.5w_t \tag{48}$$

The topography $s(x, y)$ is taken as

$$s(x, y) = \frac{s_0}{b_0}\left(\tan^{-1}\left(\frac{x^* - l_t/2}{\gamma l_t}\right) + \tan^{-1}\left(\frac{-x^* - l_t/2}{\gamma l_t}\right)\right) \times \left(\tan^{-1}\left(\frac{y^* - w_t/2}{\gamma l_t}\right) + \tan^{-1}\left(\frac{-y^* - w_t/2}{\gamma l_t}\right)\right) \tag{49}$$

where γ controls its steepness and

$$b_0 = 4\tan^{-1}\left(\frac{1}{2\gamma}\right)\tan^{-1}\left(\frac{A}{2\gamma}\right) \tag{50}$$

In all of the results which follow the initial droplet profiles are of the same form as equation (39) modified to take account of the presence of the topography, namely

$$h + s = \max\left(5\left(1 - \frac{320}{9}r^2\right), s(x, y) + h^*\right) \tag{51}$$

where r is the radial distance from the centre of the substrate.

Figures 7 and 8 show the evolution of the free surface $(h + s)$ profiles and associated contours for the flow of a completely wetting droplet, centered initially at $(x, y) = (0.5, 0.5)$, over a topographic peak $(s_0 = 0.5)$ and trench $(s_0 = -0.5)$, respectively, with $l_t = 0.2$, $A = 1$, $(x_1, y_1) = (0.3, 0.3)$ and $\gamma = 0.01$. In the former case, the droplet spreads axisymmetrically until it meets the edge of the topography when it experiences an additional pressure gradient that causes it to spread preferentially from the topography to the substrate in a direction normal to the edge of the topography. Since the droplet meets the bottom left hand corner of the topography last of all, liquid in this region is the last to experience the additional pressure gradient, causing a small cusp in the contact line in this region. In the case of the spreading over a trench, Figure 8, the edge of the topography presents an adverse pressure gradient which reduces the speed of contact line advancement across its edges and, since liquid near the bottom left hand corner is again the last to experience this adverse pressure gradient, the droplet swells slightly in its bottom left hand region.

Figures 9 and 10 show free surface profiles and associated contours for the flow of a droplet, centred initially at $(x, y) = (0.5, 0.5)$, over a topography defined by $s_0 = 0.5$, $l_t = 0.5$, $A = 1$, $(x_1, y_1) = (0, 0)$ and $\gamma = 0.01$, where the wettability on the topography differs from that of the rest of the substrate. In the former case the liquid fully wets the substrate $(\Theta_e = 0^\circ)$ while only partially wetting the topography $(\Theta_e = 11.5^\circ)$. In Figure 9 it is evident that the droplet recedes from the topography in order to increase its contact angle towards the equilibrium value of 11.5° whereas it advances on the substrate in order to lower its contact angle towards the equilibrium value of 0°. Taken together these effects cause the droplet to flow off the topography, as shown in Figure 9(c). Figure 10 shows the effect of interchanging the

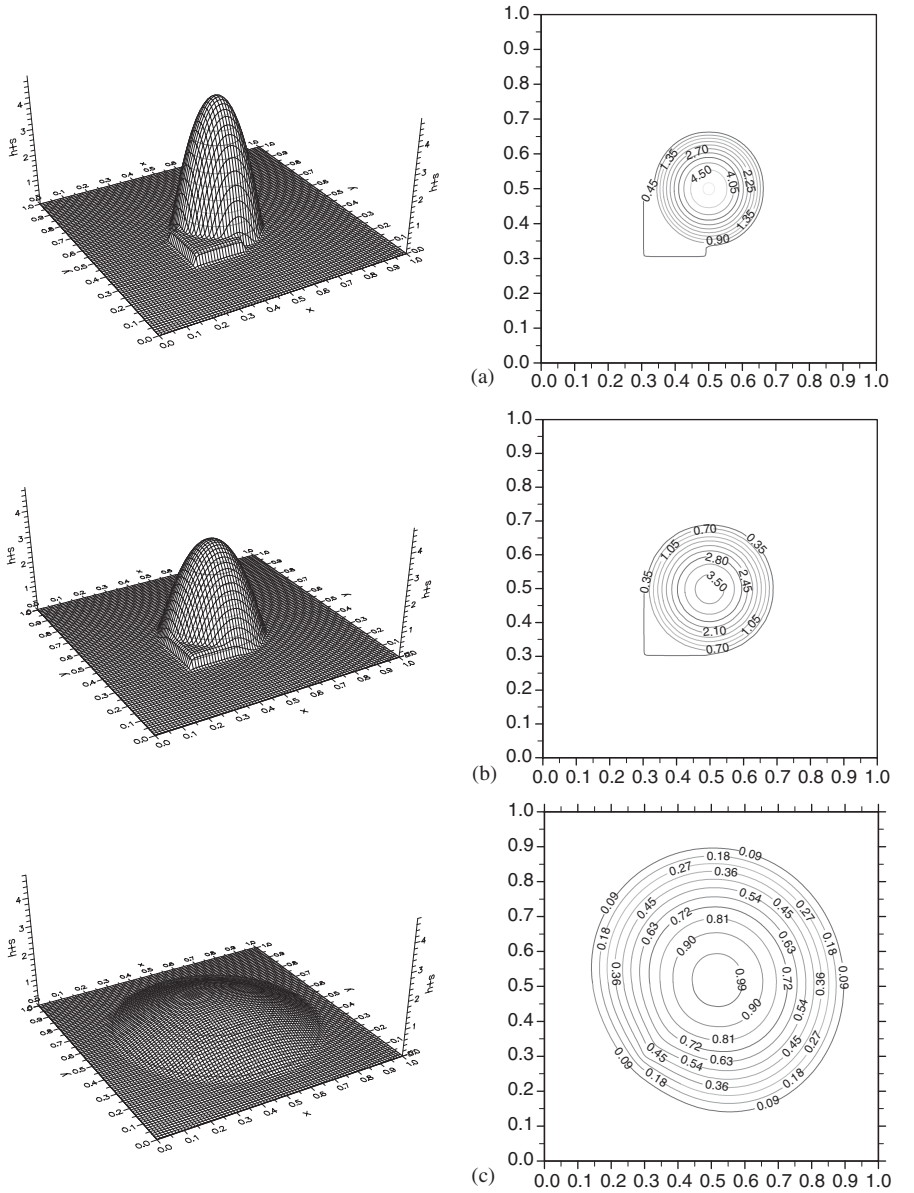

Figure 7. Free surface $(h+s)$ profiles (left) and associated contours (right) for a droplet spreading over a topographic peak with $s_0 = 0.5$, $l_t = 0.2$, $A = 1$, $(x_1, y_1) = (0.3, 0.3)$ and $\gamma = 0.01$. (a) $t = 3 \times 10^{-7}$, (b) $t = 1 \times 10^{-5}$, (c) $t = 1 \times 10^{-3}$. The density of the finest mesh is 257×257, $h^* = 0.02$ and $\mathrm{TOL} = 10^{-4}$.

wettabilities of the topography and substrate. In this case the contact line on the topography advances further across it so as to reduce the contact angle towards the equilibrium value of 0°, while that on the substrate recedes, the net effect of which is to cause the droplet to flow up (climb) onto the topographic peak, Figure 10(c).

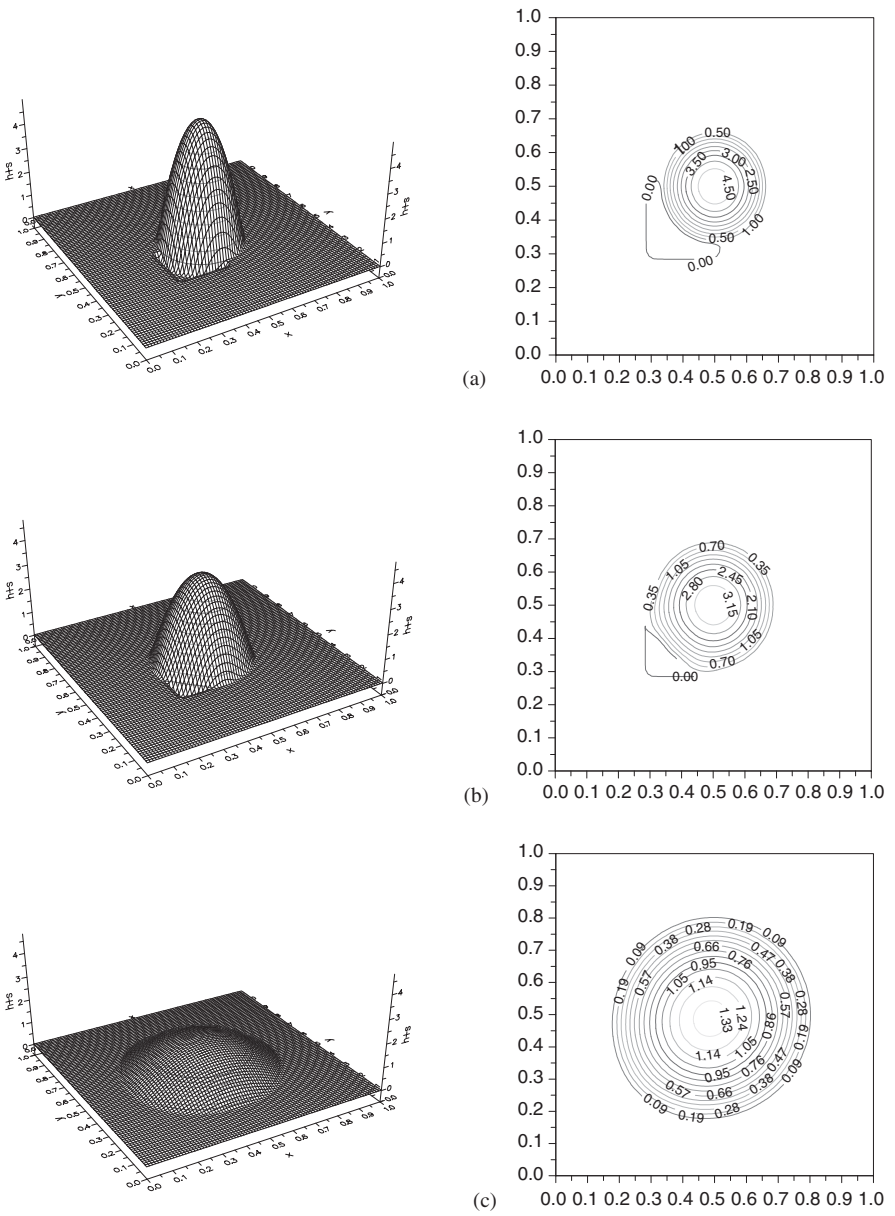

Figure 8. Free surface ($h+s$) profiles (left) and associated contours (right) for a droplet spreading over a topographic trench with $s_0 = -0.5$, $l_t = 0.2$, $A = 1$, $(x_1, y_1) = (0.3, 0.3)$ and $\gamma = 0.01$. (a) $t = 3 \times 10^{-7}$, (b) $t = 1 \times 10^{-5}$, (c) $t = 1 \times 10^{-3}$. The density of the finest mesh is 257×257, $h^* = 0.02$ and $\mathrm{TOL} = 10^{-4}$.

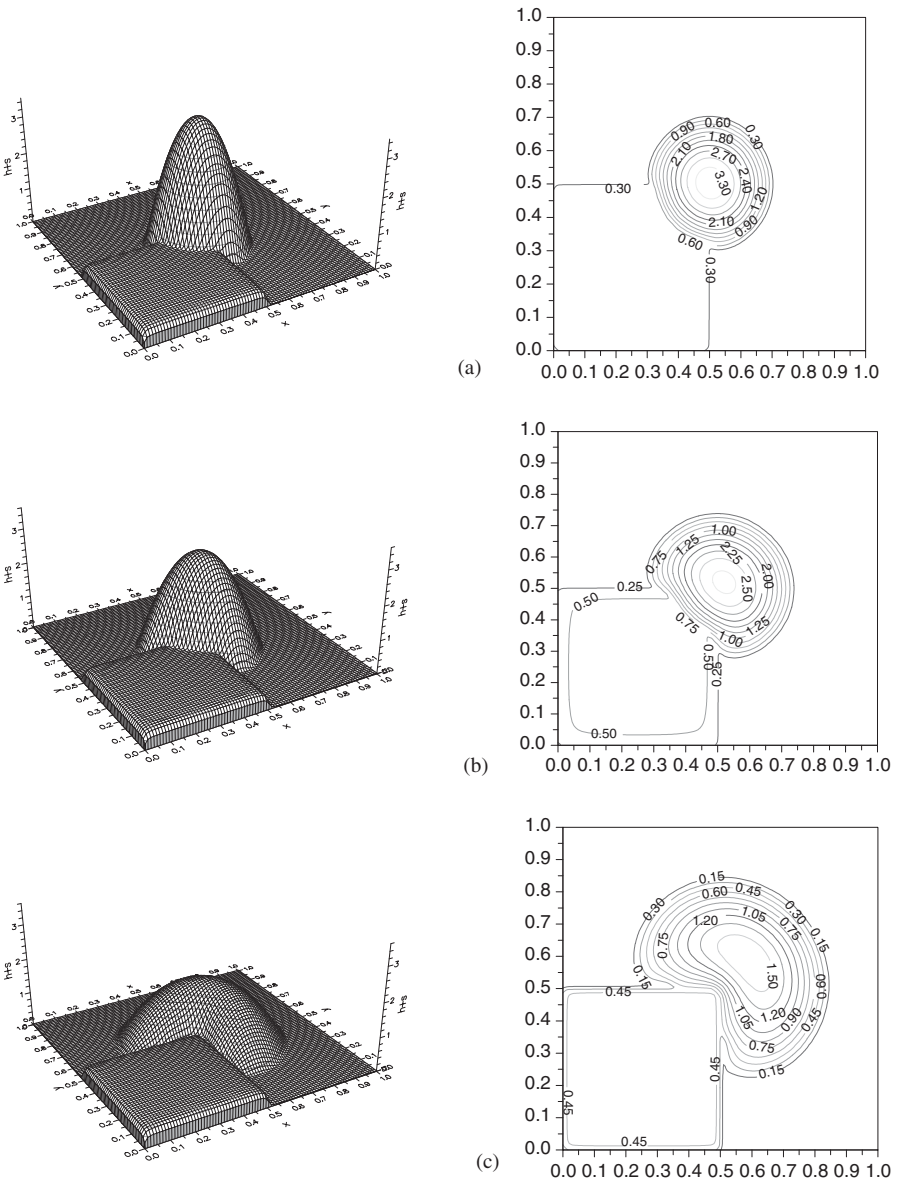

Figure 9. Free surface $(h+s)$ profiles (left) and associated contours (right) for a droplet spreading over a topographic peak with $s_0 = 0.5$, $l_t = 0.5$, $A = 1$, $(x_1, y_1) = (0.0, 0.0)$ and $\gamma = 0.01$, with $\Theta_e = 11.5^\circ$ on the topography and $\Theta_e = 0^\circ$ on the rest of the substrate. (a) $t = 1.2 \times 10^{-5}$, (b) $t = 5 \times 10^{-5}$, (c) $t = 5 \times 10^{-4}$. The density of the finest mesh is 257×257, $h^* = 0.02$ and $\mathrm{TOL} = 10^{-4}$.

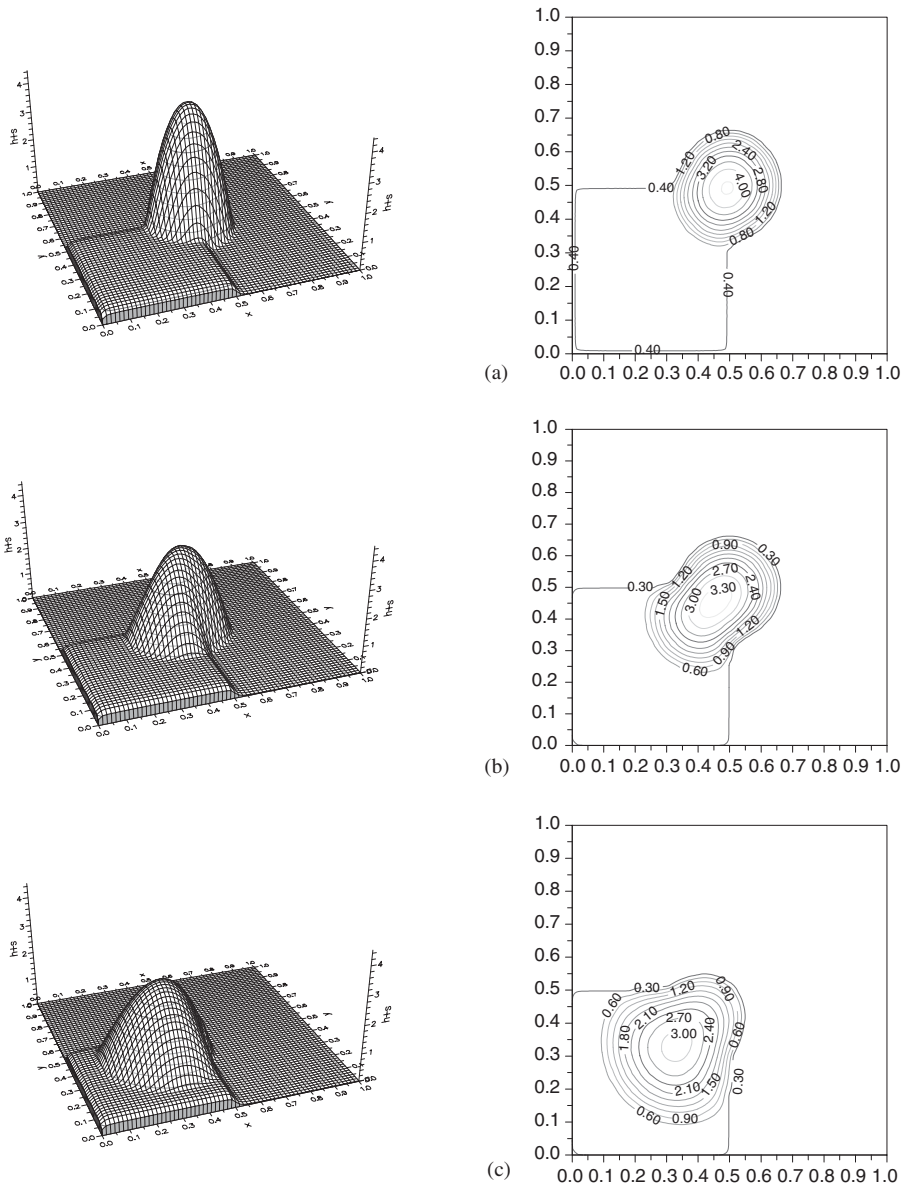

Figure 10. Free surface $(h+s)$ profiles (left) and associated contours (right) for spreading of a droplet onto a topographic peak with $s_0 = 0.5$, $l_t = 0.5$, $A = 1$, $(x_1, y_1) = (0.0, 0.0)$ and $\gamma = 0.01$, with $\Theta_e = 0^\circ$ on the topography and $\Theta_e = 11.5^\circ$ on the rest of the substrate. (a) $t = 1.2 \times 10^{-5}$, (b) $t = 1 \times 10^{-4}$, (c) $t = 5 \times 10^{-4}$. The density of the finest mesh is 257×257, $h^* = 0.02$ and $\mathrm{TOL} = 10^{-4}$.

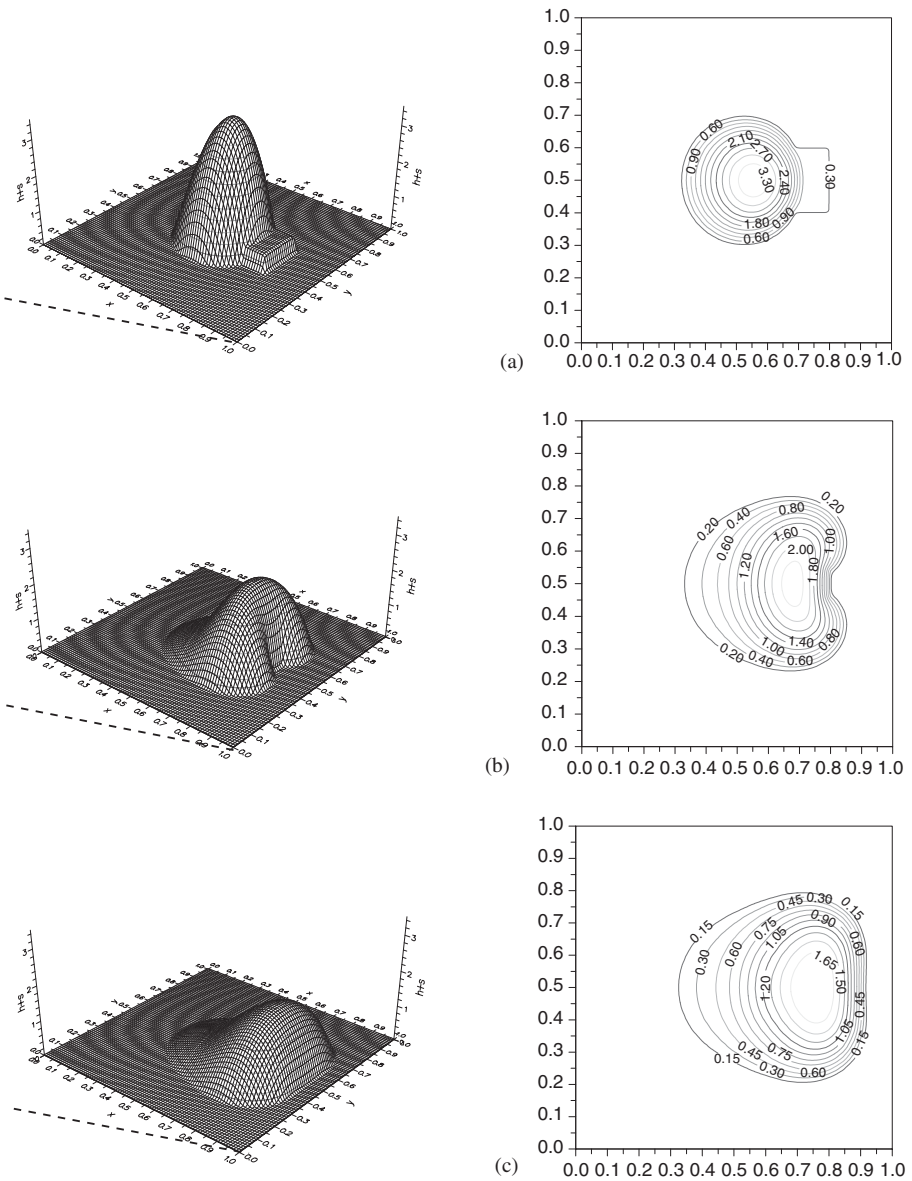

Figure 11. Free surface ($h + s$) profiles (left) and associated contours (right) for the motion of a fully-wetting droplet, down a plane inclined at 28.6° to the horizontal, over a topographic peak with $s_0 = 0.5$, $l_t = 0.2$, $A = 1$, $(x_1, y_1) = (0.6, 0.4)$ and $\gamma = 0.01$. Dotted lines indicate the inclination of the substrate with respect to the horizontal. (a) $t = 1.3 \times 10^{-5}$, (b) $t = 1.6 \times 10^{-4}$, (c) $t = 2.6 \times 10^{-4}$. Finest grid density is 257×257 and $\mathrm{TOL} = 10^{-4}$.

The last figure, Figure 11, considers the flow of a fully wetting droplet, initially centred at $(x, y) = (0.5, 0.5)$, down a plane inclined at 28.6° to the horizontal over a topographic peak defined by $s_0 = 0.5$, $l_t = 0.2$, $A = 1$, $(x_1, y_1) = (0.6, 0.4)$ and $\gamma = 0.01$. As expected, the

gravitational force causes the droplet to spread over and eventually engulf the topography. The results also show that the droplet spreads more quickly along the edges of the topography causing its contact line downstream to become heart-shaped, Figure 11(b), indeed similar free surface profiles have been reported in recent experimental and theoretical investigations of gravity-driven flows over fully submerged topographies [34, 25]. At later times the branches of the contact line behind the topography coalesce and form a straight contact line perpendicular to the direction of spreading, Figure 11(c).

5. CONCLUSIONS

The numerical solution of the time-dependent lubrication equations for the case of droplet spreading is complicated by the need to overcome, in an efficient way, the severe restrictions encountered in relation to the use of permissible time increments consequent on two main factors: stiffness introduced by surface tension and the need to resolve short length scales close to wetting lines.

The answer here, has been to develop and employ an efficient, fully implicit, multigrid solver embodying adaptive time-stepping selection, the latter optimizing the choice of time step in a controlled manner subject to a specified temporal error tolerance. A wide variety of previously reported analytical and numerical results, together with a series of new ones concerning the motion of droplets on heterogeneous substrates, have been used to validate successfully the approach.

The technological requirement for the simulation of flows past ever smaller topographic and wetting heterogeneities, and combinations of the same, makes the efficiency of such a numerical formulation extremely attractive, particularly where high resolution and hence fine meshes are essential. Firstly, time-step selection is efficient and enables the relatively small time steps required, for example, at the beginning of a simulation or when the flow is evolving quickly to be increased in a controlled and accurate manner when conditions permit. Second, the benefit of the multigrid solver is such that its fully implicit nature ensures that the larger time step estimates given by the adaptive time-stepping selection procedure can actually be used in practice, while also offering the attractive feature that the CPU time taken to solve the discretized equation set, at each time step, is simply $O(N)$ where N is the number of unknowns.

ACKNOWLEDGEMENTS

The authors wish to record their gratitude to Philips Electronics, Eindoven for sponsoring this work and to Michel Decré in particular for his keen interest in the subject matter, insightful comments and numerous helpful suggestions.

REFERENCES

1. De Gennes PG. Wetting: statics and dynamics. *Reviews of Modern Physics* 1985; **57**:827.
2. Peurrung LM, Graves DB. Spin coating over topography. *IEEE Transactions on Semiconductor Manufacturing* 1993; **6**(1):72–76.
3. Oron A, Davis SH, Bankoff SG. Long-scale evolution of thin liquid films. *Reviews of Modern Physics* 1997; **69**(3):931–980.

4. Bertozzi A. The mathematics of moving contact lines in thin liquid films. *Notices of the AMS* 1998; **45**(6): 689–697.
5. Weidner DE, Schwartz LW, Eres MH. Simulation of coating layer evolution and drop formation on horizontal cylinders. *Journal of Colloid and Interface Science* 1997; **187**(1):243–258.
6. Christov CI, Pontes J, Walgraef MG, Velarde MG. Implicit time splitting for fourth-order parabolic equations. *Computer Methods in Applied Mechanics and Engineering* 1997; **148**:209–224.
7. Weidner DE, Schwartz LW, Eley RR. Role of surface tension gradients in correcting coating defects in corners. *Journal of Colloid and Interface Science* 1996; **179**:66–75.
8. Schwartz LW, Eley RR. Simulation of droplet motion on low-energy and heterogeneous surfaces. *Journal of Colloid and Interface Science* 1998; **202**:173–188.
9. Schwartz LW. Hysteretic effects in droplet motion on heterogeneous substrates: direct numerical simulation. *Langmuir* 1998; **14**(12):3440–3453.
10. Eres MH, Schwartz LW, Roy RV. Fingering phenomena for driven coating films. *Physics of Fluids* 2000; **12**(6):1278–1295.
11. Hocking LM. Rival contact-angle models and the spreading of drops. *Journal of Fluid Mechanics* 1992; **239**:671–681.
12. Diez JA, Kondic L, Bertozzi A. Global models for moving contact lines. *Physics Reviews E* 2000; **63**:011208.
13. Wesseling P. *Introduction to Multigrid Methods*. Wiley: New York, 1992.
14. Spitaleri RM, Corinaldesi L. A multigrid semi-implicit finite difference method for the two-dimensional shallow water equations. *International Journal for Numerical Methods in Fluids* 1997; **25**:1229–1240.
15. Chou M-H. A multigrid difference approach to steady flow between eccentric rotating cylinders. *International Journal for Numerical Methods in Fluids* 2000; **34**:479–494.
16. Liao S-J, Mashayek F. A multigrid approach for steady state laminar viscous flows. *International Journal for Numerical Methods in Fluids* 2001; **37**:107–123.
17. Thompson CP, Lezeau P. Application of the full approximation storage method to the numerical simulation of two-dimensional steady incompressible viscous multiphase flows. *International Journal for Numerical Methods in Fluids* 1998; **28**:1217–1239.
18. Brandt A. Guide to multigrid development. In *Multigrid Methods: Lecture Notes in Mathematics*, Hackbusch W, Trottenberg U (eds). Springer-Verlag: Berlin, 1982; 220–312.
19. Chapra SC, Canale RP. *Numerical Methods for Engineers*. McGraw-Hill: New York, 1998.
20. Orchard SE. On surface levelling in viscous liquids and gels. *Applied Scientific Research A* 1962; **11**:451.
21. Mitlin VS. On dewetting conditions. *Colloids Surfaces A: Physicochemical Engineering Aspects* 1994; **89**: 97–101.
22. Starov VM, Kalinin VV, Chen T-D. *Advances in Colloid Interface Science* 1994; **50**:187.
23. Zhornitskaya L, Bertozzi AL. Positivity-preserving numerical schemes for lubrication-type equations. *SIAM Journal of Numerical Analysis* 2000; **37**(2):523–555.
24. Mazouchi A, Homsy GM. Free surface Stokes flow over topography. *Physics of Fluids* 2001; **13**(10): 2751–2761.
25. Gaskell PH, Jimack PK, Sellier M, Thompson HM, Wilson MCT. Gravity-driven flow of continuous thin liquid films on non-porous substrates with topography. *Journal of Fluid Mechanics* 2004; **509**:253–280.
26. Kondic L, Diez J. Pattern formation in the flow of thin film down an inclined plane: constant flux configuration. *Physics of Fluids* 2001; **13**(11):3168–3184.
27. Dormand JR. *Numerical Methods for Differential Equations—a Computational Approach*. CRC Press: Boca Raton, 1996.
28. Trottenberg U. In *Multigrid*, Trottenberg U, Oostorbe CW, Schuller A (eds) (Guest Contribution by Brandt A, Ooswald P, Stuber K). San Diego Conference. Academic Press: London, 2001.
29. Hackbusch W. *Multi-Grid Methods and Applications*. Springer: Berlin, 1985.
30. Tanner L. The spreading of silicon drops on horizontal surfaces. *Journal of Physics D* 1979; **12**:1473–1484.
31. Lelah MD, Marmur A. Spreading kinetics of drops on glass. *Journal of Colloid and Interface Science* 1981; **82**:518–525.
32. Nakaya C. Spread of fluid drops over a horizontal plane. *Journal of Physics Society Japan* 1974; **37**:539.
33. Stillwagon LE, Larson RG. Fundamentals of topographic surface levelling. *Journal of Applied Physics* 1988; **63**:5251.
34. Decré MJ, Baret J-C. Gravity driven flows of low viscosity liquids over two-dimensional topographies. *Journal of Fluid Mechanics* 2003; **487**:147–166.

